Dual-Stage K-ion Intercalation in V2O5-Conductive Polymer Composite

Journal:	*Journal of Materials Chemistry A*
Manuscript ID	TA-ART-03-2021-002003.R1
Article Type:	Paper
Date Submitted by the Author:	26-May-2021
Complete List of Authors:	Teng, Xiaowei; University of New Hampshire, Chemical Engineering Charles, Daniel; University of New Hampshire, Chemical Engineering Guo, Fenghua; University of New Hampshire, Chemical Engineering Shan, Xiaoqiang; University of New Hampshire, Chemical Engineering Kim, SaeWon; University of New Hampshire, Chemical Engineering Lebens-Higgins, Zachary; Binghamton University, Physics Xu, Wenqian; Argonne National Laboratory, X-ray Science Division, Advanced Photon Source Su, Dong; Brookhaven National Laboratory, Center for Functional Nanomaterials Piper, Louis; Binghamton University, State University of New York, Department of Physics, Applied Physics, and Astronomy

SCHOLARONE™
Manuscripts

ARTICLE

Dual-Stage K+ ion Intercalation in V2O5-Conductive Polymer Composite

Daniel S. Charles,[a] Fenghua Guo,[a] Xiaoqiang Shan,[a] SaeWon Kim,[a] Zachary W. Lebens-Higgins,[b] Wenqian Xu,[c] Dong Su, [d,e] Louis F. J. Piper,[b] Xiaowei Teng*[a]

We reported that the incorporation of conductive polymer into V_2O_5 materials resulted in an increased interlayer distance of 2.2 nm, favoring K^+ ions storage in an aqueous electrolyte. *In situ* X-ray diffraction showed that during charging, K^+ ions were first inserted into the interlayer region of V_2O_5 through pseudocapacitive intercalation and then continued to insert into $[VO_6]$ bi-layer region via diffusion-limited intercalation. This reversible dual-stage insertion/extraction mechanism provides new battery chemistry allowing to store around 50% more alkali ions in the intralayer region besides van der Waals gaps.

Introduction

Aqueous electrochemical energy storage technologies using potassium (K) ions as charge carriers and earth-abundant electrode materials are low-cost and safe alternatives to their non-aqueous counterparts for grid storage.[1-5] However, one major obstacle to large-scale implementation is their moderate storage capacity, mainly due to the large ionic radius of K-ions imposing steric hindrance in ionic transport.[6] Two-dimensional (2D) vanadium pentoxide (V_2O_5) materials, composed of edge- and corner-sharing V-O polyhedra held together by van der Waals forces, have offered ample interlayer space for hosting intercalative guest species.[7-11] Functioning V_2O_5 with guest species between layers, including alkali and, sometimes, water and even sizeable organic guest molecules, has been exploited intensively to create a more spacious gap for storing larger ions.[12-20]

Conductive polymers are important intercalative guest species to mitigate the loss of electronic conductivity in layered host materials with enlarged interlayer spacing. In oxide-conductive polymer intercalative composites, the redox-active layered metal oxide and the electrically conductive polymer combine to modify each other, leading to a new synergistic material with reinforced ionic and electronic transport for better electrochemical performance. The insertion of polymers into layered transition metal dichalcogenides has been intensively studied since the pioneering work done by Weiss and Gamble,[21, 22] but intercalative metal oxide-conductive polymer composites have only been prepared through an *in situ* polymerization with a moderate interlayer distance (~ 1.2 nm).[23-26] Here, we demonstrate the insertion of poly (3, 4 - ethylene dioxythiophene): poly (styrene sulfonate) (PEDOT: PSS) conductive polymer into the interlayer of V_2O_5 materials. The resulting intercalative V_2O_5-PEDOT: PSS (VPP) composites showed an unprecedented interlayer distance of 2.2 nm, favoring reversible K^+ ion intercalations in an aqueous electrolyte with a discharge capacity of 126 mAh g^{-1} after 100 cycles. Generally, alkali-ions are inserted into the van der Waals gap (interlayer region) through edges of the 2D layers, simultaneously causing contraction of interlayer distance due to a strengthened electrostatic interaction between positively charged alkali and negatively charged metal-oxygen polyhedra (**Fig. 1a**). Our studies demonstrate a dual-stage K-ion insertion in VPP materials, where K^+ ions are first inserted into the interlayer through pseudocapacitive intercalation and then sequentially inserted into $[VO_6]$ bi-layer (intralayer) via diffusion-limited intercalation (**Fig. 1b**). This reversible dual-stage insertion provides a new design principle for developing high-capacity layered electrode materials by engaging charge storage not only in the van der Waals gaps but also in the intralayer containing systematic structural vacancies.

Experimental Methods

Material Synthesis

Synthesis of VPP was accomplished by mixing commercial vanadium pentoxide (V_2O_5) [Sigma Aldrich 99.6% & Sigma

a. *Department of Chemical Engineering, University of New Hampshire, Durham, New Hampshire 03824, USA.*

b. *Department of Physics, Applied Physics and Astronomy, Binghamton University, Binghamton, New York 13902, USA.*

c. *X-ray Science Division, Advanced Photon Source, Argonne National Laboratory, Lemont, Illinois 60439, USA.*
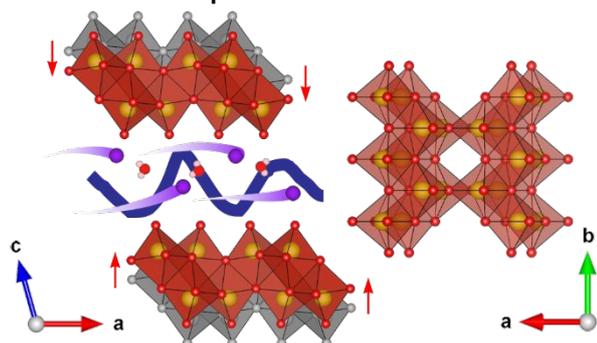
d. *Center for Functional Nanomaterials, Brookhaven National Laboratory, Upton, New York 11973, USA.*

e. *Institute of Physics, Chinese Academy of Sciences, Beijing, 100190, China.*
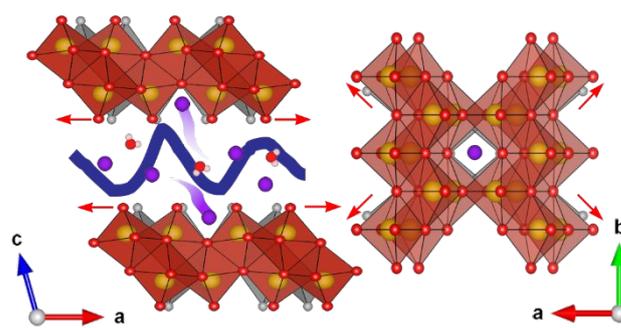
*Corresponding Author: XW.Teng@unh.edu

a Pseudocapacitive Intercalaction

Commonly Reported

b Diffusion Limited Intercalation

Reported in this Study

Figure 1. Dual-stage K-ion intercalation in VPP. (a) Pseudocapacitive intercalation of K-ions into the interlayer. (b) Diffusion limited intercalation into the intralayer.

Aldrich 99.99%) and the conductive polymer poly(3,4-ethylene dioxythiophene): poly(styrene sulfonate) [Sigma Aldrich High Conductivity Grade 3-4% in Water or Ossila High Conductivity 1% Aqueous Solution] at room temperature using a magnetic stir bar, at approximately 1000 rpm, for at least two weeks in a sealed container. A noticeable color change occurs over two weeks, ensuring the complete conversion of the raw materials. The mass ratio between V_2O_5 to PEDOT: PSS was kept at 4:1. Powder samples were obtained by washing with ethanol, centrifugation, dried in a vacuum, and then ground into a fine powder using a mortar and pestle.

Material Characterization

Transmission Electron Microscopy (TEM) images were collected with a Zeiss/LEO 922 Omega TEM, and Scanning Electron Microscope (SEM) images were collected using the Tescan Lyra3 GMU FIB-SEM at the University Instrumentation Center, University of New Hampshire. High-Resolution Transmission Electron Microscopy (HRTEM) images were collected at the Center for Functional Nanomaterials, Brookhaven National Laboratory. Thermogravimetric analysis (TGA) and Differential Scanning Calorimetry (DSC) experiments were conducted using a Mettler-Toledo instrument at the University of New Hampshire. The TGA/DSC measurement of 22 mg of VPP powder was conducted in air at a heating rate of 10°C min^{-1}.

Synchrotron X-ray Powder Diffraction (XRD) experiments were conducted at the Advanced Photon Source beamline 17-BM-B (λ=0.72768 Å and λ=0.24116 Å), Argonne National Laboratory. *Ex-situ* XRD samples were prepared in 1 mm Kapton capillaries. *In situ* XRD measurements were collected in a three-electrode cell designed at the University of New Hampshire with Kapton windows and a three-electrode half-cell configuration, and a carbon paper current collector. Three CV cycles were conducted at 1 mV s^{-1} in a 3 M KCl electrolyte.

X-ray Photoelectron Spectroscopy (XPS) measurements of VPP were collected using a Phi VersaProbe 5000 system with a monochromated Al Kα source at the Analytical and Diagnostics Laboratory (ADL) at Binghamton University. The VPP sample was mounted in a glovebox and transferred using a vacuum suitcase to avoid air exposure. The O 1s peak for the VPP sample

was shifted to match a reference α-V_2O_5 sample, which was calibrated using Au 4f7/2 peak.

The X-ray Absorption Near Edge Spectroscopy (XANES) measurements of the VPP cathodes after the charging and discharging were conducted at beamline 6-BM at the National Synchrotron Light Source II (NSLS-II) at the Brookhaven National Laboratory. The charged and discharged samples were produced by cycling in the two-electrode full cells. Cells were cycled at 0.1 A g^{-1} for ten cycles in the potential window of -0.4 to 1.4 V, followed by three cycles in the potential window of -0.4 to 1.2 V. Electrodes were rinsed with DI H_2O to remove any salt and allowed to dry. The electrode material was removed from the current collector and pressed into a pellet, and sealed with Kapton tape. The XAS data is analyzed with ATHENA software.

Electrochemistry

Cyclic voltammetry (CV) and Chronopotentiometry (CP) measurements were conducted in a three-electrode half-cell using a glassy carbon rotating disc electrode. Inks of the material consisted of 10 mg of V_2O_5 and 2.5 mg of PEDOT: PSS in 10 mL of DI H_2O. The electrodes were loaded by drop-casting 10 uL of the ink onto the rotating disc electrode. After that, active materials were covered by 20 μL of 1% Nafion solution (Sigma Aldrich) to prevent the dissolution of the electrode material. The CV measurements were conducted in a 1M KCl electrolyte (50 mL), while the CP measurements used a 3M KCl electrolyte. For all half-cell measurements, the electrolyte solutions were bubbled with inert Ar gas and were measured in the potential window of -0.1 to 0.9 V vs. a saturated Ag/AgCl reference electrode using the CHI 660E potentiostat and Pine RDE.

Electrochemical Impedance Spectroscopy and Current-Pulse Relaxation measurements were conducted in a three-electrode half-cell at open-circuit voltage using a glassy carbon electrode and an Ag/AgCl reference electrode in 50 mL 1 M KCl electrolyte. The frequency range used in the EIS measurements was 0.1 Hz to 100 kHz with an A.C. amplitude of 5 mV. The current-pulse relaxation measurement used a 20 ug loading of active materials, and a positive current pulse of 5x10^{-6} A was applied for 15 seconds.
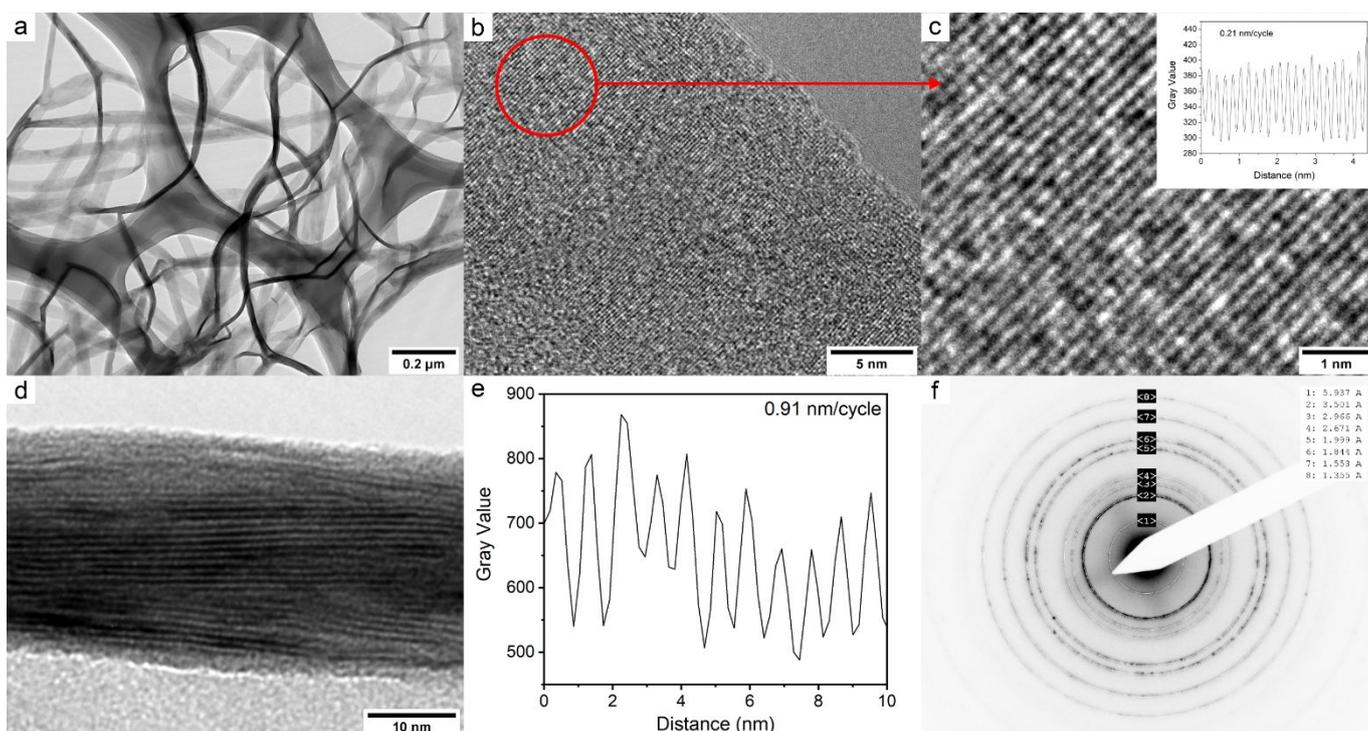
Figure 2. Transmission Electron Microscopy of VPP. (a) TEM showing the nanoribbon morphology. (b) HRTEM image, and (c) HRTEM image of the fringe showing the ordered structure. (d) TEM image of a twist of a VPP nanoribbon exposing the layered structure. (e) Calculation of Interlayer spacing from TEM image shown in (d). (f) Electron diffraction pattern of VPP.

CP measurements using two-electrode asymmetric full cells were collected using active carbon anodes (20 mg), VPP/carbon cathode (0.4 mg/1.6 mg), filter paper separator, and 3M KCl (300 uL) as the electrolyte. Higher concentration KCl was used for CP than CV measurements to minimize possible transport limitation. Cells were cycled using Arbin and Solartron potentiostat in EL-Cell ECC-Aqu electrochemical cells between -0.4 and 1.4 V at 0.05, 0.1 and 0.2 A g^{-1} and between -0.4 and 1.2 V at 0.5, 1.0, and 2.0 A g^{-1}. A small portion of the electrolyte was sacrificed on the initial charging cycles as neither the VPP cathode nor the overloaded carbon anode is initially a source of K$^+$ ions. During the startup process, as K$^+$ ions being stored at the anode and the OER reaction occurring at the cathode, the relative potential window shifts to a lower absolute potential.

Results and Discussion

Intercalative VPP was synthesized using a dissolution and recrystallization method in an aqueous solution containing bulk V$_2$O$_5$ particles and PEDOT: PSS at room temperature. Conversion of bulk V$_2$O$_5$ particles into ribbon-like VPP nanostructures occurred with distinct changes in morphologies and atomic structures. **Figure 2a** shows TEM images of VPP nanoribbons. Unlike the micron-sized commercial V$_2$O$_5$ particles (**Fig. S1**), VPP materials show web-like entanglements consisting of one-dimensional (1D) ribbon-like structures. High-resolution TEM shows that VPP nanoribbons are crystalline materials (**Fig. 2b & c**). The distances between lattice fringes are deduced to be 2.1 Å. Some VPP layered structures have curled edges, and therefore the interlayer distance of the

nanoribbons can be calculated. **Figure 2d** shows an assembly of several twisted VPP nanosheets with the side of the nanoribbon exposed. An average interlayer distance of 0.91 nm was calculated (**Fig. 2e**). It should be noted that the PEDOT: PSS and water molecules might have been removed from the interlayer of VPP under the high vacuum imaging, and the resultant 0.91 nm interlayer spacing is typical for this type of bilayer vanadium oxides. The electron Diffraction pattern from the selected area of VPP is shown in **Figure 2f**, the (200), (110), and (020) planes are in good agreement with results from XRD. Figure S2 shows the results from thermogravimetric analysis (TGA) and differential scanning calorimetry analysis (DSC). Two typical endothermic heat flow peaks from water evaporation and vanadium melting appear at ~100 °C and ~660 °C, respectively. A major exothermic peak at ~ 425°C and a satellite peak at ~ 300 °C can be attributed to the combustion of PEDOT: PSS. From the extent of the mass decreases, the structural water accounts for 12.7 % and PEDOT: PSS accounts for 16.1 % of the total mass, the vanadium and structural water is estimated to be V2O5 · 1.8 H$_2$O.

The synchrotron XRD of VPP is indexed as δ-Ax V$_2$O$_5$·nH$_2$O (A = none, Li, Na, K, Ca, NH$_4$, VO$_x$, Ni, and polyaniline among others).[27-32] It has a monoclinic unit cell with C$_{2/m}$ symmetry with a bi-layered structure consisting of [VO$_6$] polyhedra in zig-zag chains with angular tunnels in [VO$_6$] layers (**Fig. 3a**).[29, 33, 34] In stark contrast, the commercial bulk V$_2$O$_5$ is highly crystalline identified as α- V$_2$O$_5$ (**Fig. S3**). The intense XRD peak of VPP at Q=0.44 Å^{-1} (Q, momentum transfer, is the magnitude of the scattering vector, **Eq. 1**) is from the lamellar diffraction plane (001) with a corresponding d-spacing (d$_{001}$) of 14.2 Å.
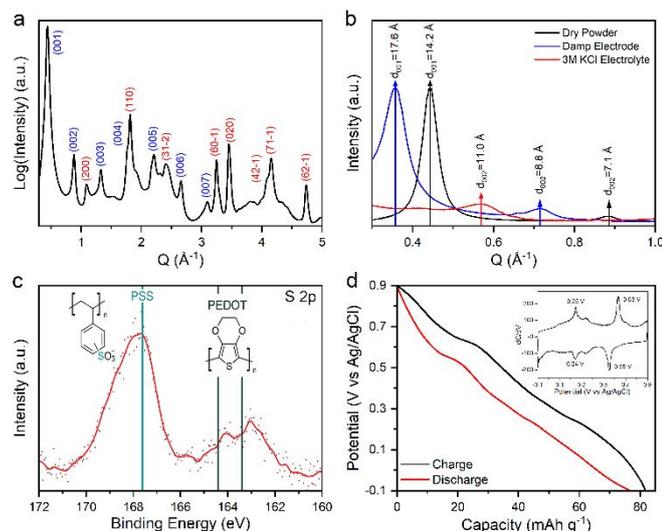
Figure 4. Structural and electrochemical characterization of VPP materials. (a) synchrotron XRD indexed as a monoclinic unit cell with $C_{2/m}$ symmetry. (b) Synchrotron XRD of VPP at various hydration states, including dry powder, damp drop-cast electrode, and submerged electrode in an aqueous 3 M KCl electrolyte. (c) XPS of the S-2p region. (d) CP at 0.2 A g^{-1} in a 3 M KCl electrolyte with the inset containing the differential capacity (dC/dV) measured in a three-electrode half-cell.

Such wide interlayer spacing is indicative of the insertion of large molecules between the layers, consistent with previously reported V_2O_5 with intercalative PEDOT made from *in situ* polymerization methods.[35-37] The (00l) lamellar reflections (l: from 1 to 7) are indexed in blue. **Figure 3b** shows the XRD patterns of VPP materials in the form of vacuum-dried powder (black), damp electrode containing water from the slurry formulation that was then al-lowed partially dry in air (blue), and hydrated powder upon the interaction between the KCl electrolyte (red) before electrochemical cycling. The XRD results show that VPP experienced a significant increase of interlayer distance during the above processes, much like vanadium oxide gels, where the d001 increased from 14.2 Å to 17.6 Å after exposure water in the slurry formulation and being dried in air. Finally, the interlayer distance increased to 22.0 Å while immersed in the KCl electrolyte. Notably, the increase of d_{001} should be attributed to the insertion of the water instead of K^+ ions into the interlayers, as the latter would cause contracted interlayer spacing due to increased electrostatic interaction. The VPP materials were analyzed by Fourier-transform infrared spectroscopy (FTIR) measurements, showing V-O-V and V=O vibrations (**Fig. S4**). The intercalative nature of PEDOT: PSS into the interlayer of the VPP materials was further demonstrated by XPS analysis of the S-2p spectra. **Figure 3c** shows that thoroughly washed VPP has two distinct S-2p features at ~ 164.0 eV and 167.6 eV, corresponding to the PEDOT (thiophene) and the PSS ($SO3^-$), respectively.[39, 40] Unlike bulk α-V_2O_5 with a dominant V^{5+}, VPP shows an increased V^{4+} with the $V2p_{3/2}$ peaks at 517.6 eV and 516.3 eV in V-2p O-1s region (**Fig. S5**), corresponding to V^{5+} and V^{4+}, respectively.[41]

Three-electrode half-cell measurements were conducted in a KCl electrolyte from -0.1 V to 0.9 V (vs. Ag/AgCl). CP measurements of VPP demonstrated a discharge capacity of 76 mAh g^{-1} at a current density of 0.2 A g^{-1} (**Fig. 3d**). Plateaus in the

charging curves (~ 0.25 V and ~0.63 V) and discharge curves (~ 0.55 V and ~0.24 V), determined by the dC/dV plot, agree well with redox features in the CV scans (**Fig. S6a**). CV measurements showed much enhanced K^+ ion electrochemical storage in VPP, compared to that in bulk V_2O_5 and PEDOT: PSS (**Fig. S6 c-d**). The long-term cycling of VPP is evaluated in a two-electrode cell, composed of an active carbon electrode as an anode (**Fig. S7**). The VPP cathode materials show excellent discharge capacities of 126, 114, and 91.0 mAh g^{-1} at current densities of 0.05, 0.1, and 0.2 A g^{-1} after 100 cycles, respectively, as well as average capacity retention of 87% and an average coulombic efficiency of 89%. The capacity contribution from conducting carbon is negligible (**Fig. S8**). Notably, the relatively low coulombic efficiency (89%) is attributed to the gas evolution reactions, confirmed by dC/dV plot (**Fig. S9**). By reducing the upper voltage limit and thus the overall voltage window, gas evolution reactions are significantly mitigated. The coulombic efficiency can be improved to be over 95%, as shown in **Figure S10**, though the discharge capacities are slightly decreased from 120 to 102 mAh g^{-1} at current densities of 0.1 A g^{-1}. Extended cycling in the potential window of -0.4 to 1.4 V was carried out at current densities of 0.5 1.0 and 2.0 A g^{-1}, shown in **Figure S11**. The cells operated at these conditions exhibited coulombic efficiencies greater than 95%.

Electrochemical impedance spectroscopy was used to measure the resistance to charge transfer (R_{ct}) of VPP and bulk V_2O_5 materials (**Fig. S12**). VPP and bulk V_2O_5 exhibited a similar solution and contact resistance (~ 10 ohms), but VPP showed a much smaller charge transfer resistance (~1 ohm) at the electrode-electrolyte interface than V_2O_5 (3.5 ohms). We also
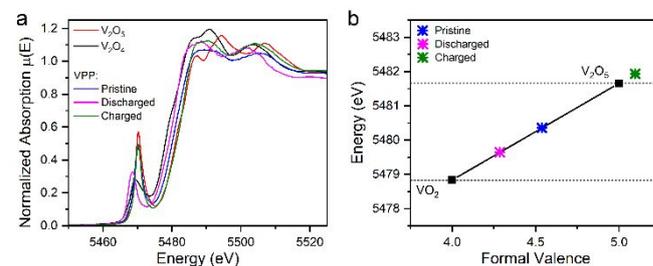

Figure 3. (a) Vanadium K-edge XANES spectra of VPP at the pristine, charged, and discharged states, along with V_2O_5 and V_2O_4 standards. (b) Formal oxidation states of VPP at the various states.

used a current-pulse relaxation method to calculate the solid-state diffusion coefficients for K^+ ions in VPP and V_2O_5, respectively (**Fig. S13**).[42] The results showed that the K^+ ion diffusion coefficient in VPP was approximately 2.5 times higher than that of bulk V_2O_5. Both measurements suggested that PEDOT: PSS incorporated into the interlayer of VPP materials leads to a faster diffusion of K^+ ions.

Figure 4 shows the electronic structures of VPP materials at pristine, charged, and discharged states, analyzed by the vanadium K-edge XANES. Due to the low absorption energy of vanadium K-edge and the strong absorption of aqueous electrolyte, VPP materials were t fully charged and discharged in two-electrode full-cells and then rinsed and dried for *ex-situ* XANES analysis. The discharged VPP shows the half-edge step [½ $\mu(E_0)$] at a lower absorption energy position than charged
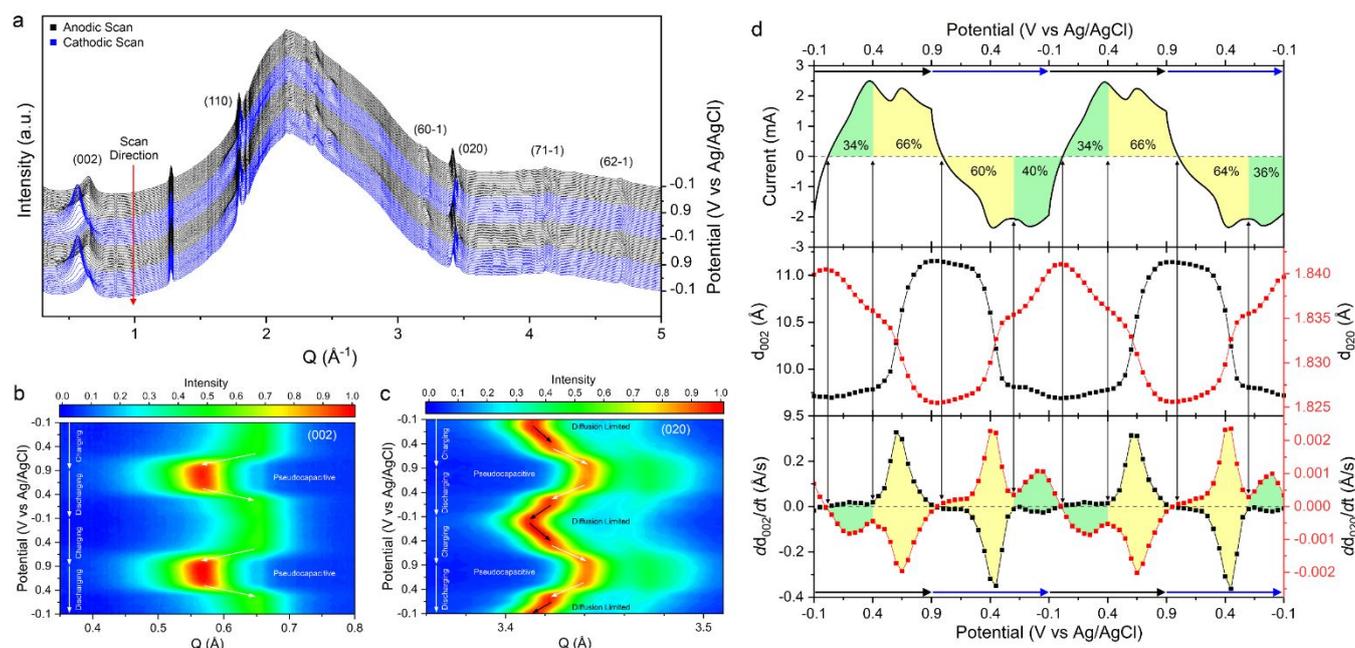
Figure 5. In situ synchrotron XRD of VPP. (a) Full XRD scans collected during electrochemical cycling in a 1.0 V potential window (-0.1 to 0.9 V vs Ag/AgCl) at 1 mV s-1 in a 3 M KCl electrolyte. Contour plots showing the evolution of the (b) (002) and (c) (020) peaks of VPP during cycling. (d) The CV curves, the evolution of d-spacing, and the rate of change (ddhkl/dt) for the (002) and (020) peaks. K-ions storages in the interlayer and intralayer regions are highlighted in yellow and green, respectively.

VPP, suggesting a more reduced electronics state. Compared to spectra from V_2O_5 and V_2O_4 standards, the change of energy position at the half-edge step between charged and discharged VPPs suggests a valence change of 0.76 charge transfer per vanadium atom, in agreement with the capacity values obtained from full-cell measurements. This indicates the vanadium valence in VPP experienced transitions between V^{4+} and V^{5+} during discharging and charging processes. Notably, the electronic structure of the vanadium atom and its local coordination environment can also be revealed from the pre-edge features. The discharged VPP showed a much decreased pre-edge intensity than charged one and suggested a reduced electronic statement, congruent with an increasing ratio of vanadium species with high local symmetry (VO_6 units) when electrons filled the hybridized 3d-2p states upon the K^+ ion intercalation.

The *in situ* synchrotron XRD of VPP during CV cycling is shown in **Figure 5**. The second and third cycles of the CV are overlapped, suggesting the highly reversible insertion and extraction of K^+ ions during the initial cycling (**Fig. S8**). The contour plots in **Figure 5b & c** shows the (002) and (020) peaks moving in opposing directions during cycling, corresponding to changes of interlayer spacing and V-O distance in the bi-layer (b-lattice constant), respectively. From the contour plot, the (002) peak evolution shows a rapid expansion and contraction. In contrast, the (020) peak undergoes both expansion and contraction in two distinct stages. **Figure 5d** shows the changes of d_{002} and d_{020}, rates of changes (dd_{hkl}/dt), and the current response from the CV, all as functions of the potential. During the cathodic scan (blue arrows), the applied potential decreased from 0.90 V to 0.25 V, promoting the insertion of K^+ ion into VPP (highlighted in yellow). The d_{002} decreased from 11.160 Å to 9.805 Å due to a strengthened electrostatic

interaction between $[VO_6]$ bi-layers (intralayer) and K^+ ions inserted in van der Waals gaps (interlayer).[7, 43, 44] Meanwhile, the d_{020} increased from 1.825 Å to 1.835 Å due to an increased portion of V^{4+} with a longer V-O bond distance.[10] The changes of (002) and (020) coincide at the same potential (0.40 V), reaching a minimum and maximum, respectively.

Uniquely, when potential continuously decreases from 0.25 V to -0.10 V (highlighted in green in **Fig. 5d**), further K^+ ion insertion into VPP has a proportionally more significant effect on the intralayer, where d_{020} experiences an expansion from 1.835 Å to 1.841 Å (37.5 % of overall changes during reduction), compared to d_{002} from 9.805 Å to 9.689 Å (7.9 % of the overall changes). The dd_{hkl}/dt curves also manifest this two-stage behavior. The derivative of d_{020} during the cathodic scan (blue arrows) has two positive peaks (~0.4 V and ~0 V), while the derivative of d_{002} has a single negative peak (~0.4 V). Two derivative peaks indicate that K-ion insertion occurs in two distinct stages. In the first stage, from 0.90 V to 0.25 V (yellow in **Fig. 5d**), K-ions inserted into the interlayer of VPP from the electrolyte, accounting for 60% of the overall discharge capacity. In the second stage, from 0.25 V to -0.10 V (green), K-ions from the interlayer inserted into the intralayer, accounting for 40% of the overall discharge capacity. Inversely, during the anodic scan (black arrows), the derivative of d_{002} has one positive peak (~0.6 V), and the derivative of d_{020} has two negative peaks (~0.2 V and ~0.6 V). It suggests a similar two-stage behavior during K^+ ion extraction, during which K^+ ions first diffuse from the intralayer to the interlayer from -0.10 V to 0.40 V (green), accounting for 36% of the overall charging capacity; consequently, K^+ ions extract from interlayer to electrolyte via the edge from 0.40 V to 0.90 V (yellow), accounting for 64% of the overall charging capacity. Collectively, the intralayer of VPP could host around 50% of K-ions that the

interlayer region could store. Notably, when K-ions diffused from the interlayer to the intralayer, d_{002} remains unchanged, suggesting some K^+ ions are continuously inserted into the interlayer from the electrolyte.

In addition to (002) and (020) diffraction peaks, the evolution of several other peaks was examined during electrochemical cycling, including (110), (60-1), (71-1), and (62-1) (**Fig. S14**). The changes to the d-spacing (d_{hkl}) and dd_{hkl}/dt are shown in **Figure S15**. The changes of the additional four diffraction peaks unambiguously demonstrate dual-stage K^+ ion storage, congruent with the conclusion drawn by studying (002) and (020) peak changes. Moreover, our comprehensive analysis further reveals that diffraction peaks indexed with (h k 0), such as (020) and (110) have a monotonic d_{hk0} change: namely, d_{hk0} increases on discharging and decreases on charging. However, peaks indexed with (h k l, l≠0,), such as (60-1) and (71-1), show that d_{hkl} changes in both directions within a single CV segment. For example, on discharging, d_{60-1} first decreases as K^+ ions are inserted into VPP interlayer spacing and then increases as K-ions are inserted from the interlayer into the intralayer during the same discharging CV segment. These results further manifest the delicate influence of such dual-stage K^+ ion intercalation on the crystallography of VPP: when K^+ ions are inserted into interlayer on discharging, crystallographic planes with high h, such as (60-1) and (71-1) are strongly affected by l value and thus shows a decreased d_{hkl} because interlayer distance decreases significantly. On the other hand, when K-ions are inserted from the interlayer into the intralayer, h, k and l are all affected by a reduced valence state of vanadium, thus showing an increased d_{hkl}. This is because V-O bond distance increases
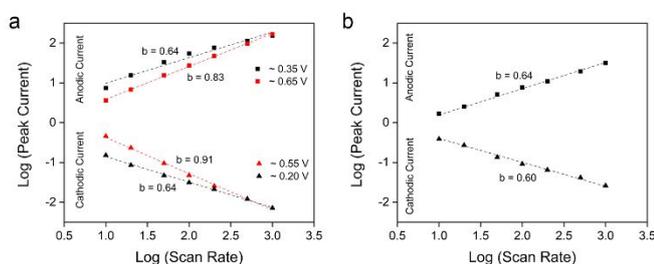
Figure 6. Electrokinetic analysis of (a) VPP and (b) bulk V2O5 using cyclic voltammetry data using the "b-value" calculation.

sharply in the 2nd stage of K-ion insertion, while interlayer distance remains nearly constant.

Electro-kinetic analysis of the CVs at various scan rates (v) reveals the K^+ ion storage mechanisms at each stage. The redox peak current (i_{peak}) varies as $v^{1/2}$ for a redox reaction limited by semi-infinite diffusion and varies as v for a capacitive process. This relation is expressed in **Eq. 2**, with the value of b providing insight into the charge storage mechanism. **Figure 6a** shows that the anodic peak current at ~ 0.7 V has a b-value of 0.83, and the corresponding cathodic peak current at ~ 0.5 V has a b-value of 0.91. The high b-value implies that K^+ ions insert into (or extract from) interlayer through a capacitive process (so-called pseudocapacitive intercalation).[45] Conversely, the anodic peak current at 0.4 V and cathodic peak current of 0.1 V have a much lower b-value of 0.64, suggesting a diffusion-limited process when K^+ ion insert into the intralayer from the

interlayer or extract from the intralayer to the interlayer. The results of the electro-kinetic analysis correspond well with the observed structural changes from the *in situ* XRD.

In comparison, bulk V_2O_5 material only has one redox couple in the 1 V potential window and shows a *b*-value of 0.64 in the anodic scan and 0.6 in the cathodic scan (**Figure 6b**). The similar *b*-values for the bulk V_2O_5 and lower potential redox peak of VPP (when K^+ ions are inserted into intralayer from interlayer) indicate the insertion of K^+ ions into bulk V_2O_5 and the intralayer (within the bi-layer) of VPP is kinetically similar. This conclusion agrees well with the atomic structure of the bulk V_2O_5 and the
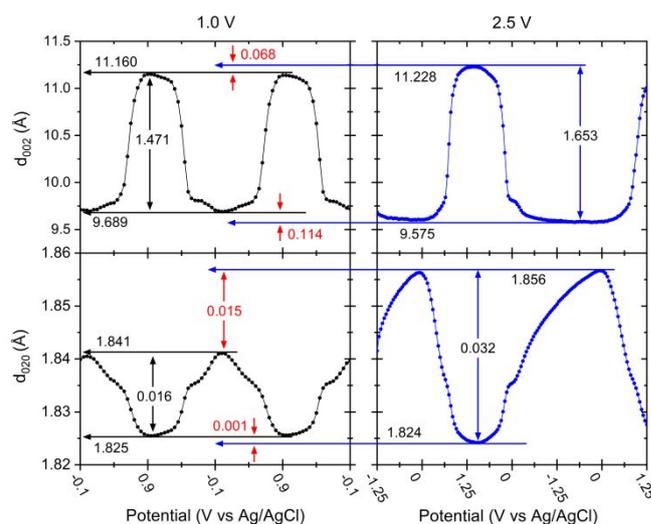
Figure 7. Comparison of the (002) and (020) in situ X-ray diffraction peak evolution at 1.0 V and 2.5 V potential windows.

bi-layer region of the VPP, where densely packed atoms impose a barrier for K^+ ion transport via a diffusion-limited process.

More evidence on the dual-stage K^+ ion intercalation in VPP is obtained from *in situ* XRD conducted under an extended potential window of 2.5 V (**Fig. S16 & S17**). An expanded potential window of 2.5 V was used to highlight the different intercalation mechanisms by further discharging VPP. While operation at this condition is not feasible due to the significant gas evolution reactions, the 2.5-V-voltage window provides valuable information on how the crystalline structure changes upon continuous K^+ ion insertion. **Figure 7** shows that under a 2.5 V-voltage-window, the changes of d_{002} undergo a minor increase of 12.4 % relative to that at a 1.0 V potential window, suggesting that K^+ ion concentrations in the interlayer region remained relatively constant. In contrast, the changes of d_{020} experience a significant increase of 106.9% relative to that under 1.0 V, suggesting that the intralayer region could host more K^+ ions as potential continues to decrease (higher overpotential for K^+ ion intercalation). This strong-potential-dependent evolution of d_{020} also suggests the K^+ ion intercalation from interlayer to intralayer is transport-limited, congruent with the electro-kinetics analysis.

We attribute this unique diffusion-limited intercalation of K^+ ion from the interlayer into the intralayer to the systematic vacancies in the $[VO_6]$ bi-layers (**Fig 1b**). **Figure S18** shows the *in situ* XRD measurements of crystalline layered $K_{0.33}V_2O_5$, highly

disordered layered $K_{0.22}V_2O_5 \cdot 0.8H_2O$, and δ- $Na_{0.27}MnO_2 \cdot 0.8H_2O$ birnessite layered materials.[10, 18, 46, 47] Notably, all three materials have layered structures with a monoclinic unit cell with a $C_{2/m}$ symmetry and an interlayer spacing of around ~ 1 nm. Similar to VPP, both layered V_2O_5 materials, regardless of their disordered or crystalline structure, have systematic vacancies in the V-O bi-layers and exhibit the dual-stage intercalation mechanism, though less distinct than VPP. On the other hand, dual-stage intercalation is absent in $Na_{0.27}MnO_2$ birnessite with close-packed Mn-O layers without systematic vacancies. Lastly, we want to point out that the insertion of Li- and Na- ions into the $NH_4V_4O_{10}$ intralayer has been predicted by theoretical calculations in a non-aqueous energy storage system.[48] Our results not only complement the previous theoretical studies by experimentally validating the K^+ ions insertion into the interlayer of bi-layered vanadium oxides but, more importantly, demonstrate such a dual-stage insertion mechanism in aqueous energy storage, which has never been reported before.

Conclusions

Our structural and electrochemical characterizations reveal dual-stage K^+ ion intercalation (pseudocapacitive and diffusion-limited intercalation) in VPP materials, where K^+ ions were first inserted into the interlayer region and the continuous reduction caused the insertion of K^+ ions from the interlayer into the intralayer, enabled by the angular tunnels in the $[VO_6]$ bi-layer. The dual-stage K^+ ion insertion/extraction in VPP is collectively evidenced by the changes of various d_{hkl} via *in situ* XRD measurements conducted at two different potential windows, as well as the electro-kinetic analysis. Our results shed light on discovering the new intercalation mechanism in bi-layered vanadium oxides, in which the interlayer spacing and the bi-layer region can host alkali-ions. Since bi-layer vacant sites could host at least an additional 50% of charges stored in the interlayer region, our studies provide a route towards developing high capacity electrodes by tailoring the polyhedral layers of materials with van der Waal gaps for optimal storage performance.

Author Contributions

D.S.C. contributed to the material synthesis, structural characterizations, and electrochemical measurements, as well as manuscript preparation. F.G. and S.K contributed to full-cell measurements. X.S. and W.X. contributed to *in situ* XRD experiments. Z.L.H. and L.P. contributed XPS measurements and discussion. D.S. contributed HRTEM measurements. X.T. contributed to the manuscript preparation and research supervision.

Conflicts of interest

The authors declare no competing financial interests.

Notes and references

1. H. Kim, J. Hong, K. Y. Park, H. Kim, S. W. Kim and K. Kang, *Chem Rev*, 2014, **114**, 11788-11827.
2. X. Shan, D. S. Charles, Y. Lei, R. Qiao, G. Wang, W. Yang, M. Feygenson, D. Su and X. Teng, *Nat. Commun.*, 2016, **7**, 13370.
3. D. Sun, L. Jin, Y. Chen, J.-R. Zhang and J.-J. Zhu, *ChemPlusChem*, 2013, **78**, 227-234.
4. M. Pasta, C. D. Wessells, R. A. Huggins and Y. Cui, *Nat. Commun.*, 2012, **3**, 1149.
5. M. Pasta, C. D. Wessells, N. Liu, J. Nelson, M. T. McDowell, R. A. Huggins, M. F. Toney and Y. Cui, *Nat. Commun.*, 2014, **5**, 3007.
6. M. Tian, Y. Gao, Z. Wang and L. Chen, *Phys. Chem. Chem. Phys.*, 2016, **18**, 17345-17350.
7. B. Tian, W. Tang, C. Su and Y. Li, *ACS Appl Mater Interfaces*, 2018, **10**, 642-650.
8. L. R. De Jesus, J. L. Andrews, A. Parija and S. Banerjee, *Acs Energy Letters*, 2018, **3**, 915-931.
9. G. A. Horrocks, A. Parija, L. R. De Jesus, L. Wangoh, S. Sallis, Y. Luo, J. L. Andrews, J. Jude, C. Jaye, D. A. Fischer, D. Prendergast, L. F. J. Piper and S. Banerjee, *Chemistry of Materials*, 2017, **29**, 10386-10397.
10. D. S. Charles, M. Feygenson, K. Page, J. Neuefeind, W. Xu and X. Teng, *Nat. Commun.*, 2017, **8**, 15520.
11. I. E. Rauda, V. Augustyn, L. C. Saldarriaga-Lopez, X. Chen, L. T. Schelhas, G. W. Rubloff, B. Dunn and S. H. Tolbert, *Advanced Functional Materials*, 2014, **24**, 6717-6728.
12. Y. Lu, L. Wang, J. Cheng and J. B. Goodenough, *Chem. Commun.*, 2012, **48**, 6544-6546.
13. S. Guo, Q. Li, P. Liu, M. Chen and H. Zhou, *Nat. Commun.*, 2017, **8**, 135.
14. J. Zheng, P. Yan, W. H. Kan, C. Wang and A. Manthiram, *Journal of The Electrochemical Society*, 2016, **163**, A584-A591.
15. C. D. Wessells, R. A. Huggins and Y. Cui, *Nat. Commun.*, 2011, **2**, 550.
16. C. D. Wessells, S. V. Peddada, R. A. Huggins and Y. Cui, *Nano Lett*, 2011, **11**, 5421-5425.
17. Y. He, W. Chen, X. Li, Z. Zhang, J. Fu, C. Zhao and E. Xie, *ACS Nano*, 2013, **7**, 174-182.

18. M. P. Yeager, W. Du, B. Bishop, M. Sullivan, W. Xu, D. Su, S. D. Senanayake, J. Hanson and X. Teng, *ChemSusChem*, 2013, **6**, 2231-2235.

19. L. Peng, X. Peng, B. Liu, C. Wu, Y. Xie and G. Yu, *Nano Lett*, 2013, **13**, 2151-2157.

20. M. Clites and E. Pomerantseva, *Energy Storage Materials*, 2018, **11**, 30-37.

21. A. Weiss and R. Ruthardt, *Zeitschrift Fur Naturforschung Part B-Chemie Biochemie Biophysik Biologie Und Verwandten Gebiete*, 1969, **B 24**, 355-&.

22. F. R. Gamble, F. J. Disalvo, R. A. Klemm and T. H. Geballe, *Science*, 1970, **168**, 568-570.

23. M. G. Kanatzidis, L. M. Tonge, T. J. Marks, H. O. Marcy and C. R. Kannewurf, *J. Am. Chem. Soc.*, 1987, **109**, 3797-3799.

24. M. G. Kanatzidis, C. G. Wu, H. O. Marcy, D. C. Degroot and C. R. Kannewurf, *Chemistry of Materials*, 1990, **2**, 222-224.

25. M. G. Kanatzidis, C. G. Wu, H. O. Marcy and C. R. Kannewurf, *J. Am. Chem. Soc.*, 1989, **111**, 4139-4141.

26. Y. P. Chen, G. Yang, Z. H. Zhang, X. Y. Yang, W. H. Hou and J. J. Zhu, *Nanoscale*, 2010, **2**, 2131-2138.

27. Y. Oka, T. Yao and N. Yamamoto, *Journal of Solid State Chemistry*, 1997, **132**, 323-329.

28. T. Yao, Y. Oka and N. Yamamoto, *J. Mater. Chem.*, 1992, **2**, 331-336.

29. T. Yao, Y. Oka and N. Yamamoto, *J. Mater. Chem.*, 1992, **2**, 337-340.

30. V. Petkov, V. Parvanov, P. Trikalitis, C. Malliakas, T. Vogt and M. G. Kanatzidis, *J Am Chem Soc*, 2005, **127**, 8805-8812.

31. P. N. Trikalitis, V. Petkov and M. G. Kanatzidis, *Chemistry of Materials*, 2003, **15**, 3337-3342.

32. W. Chen, Q. Xu, Y. S. Hu, L. Q. Mai and Q. Y. Zhu, *Journal of Materials Chemistry*, 2002, **12**, 1926-1929.

33. V. Petkov, P. N. Trikalitis, E. S. Bozin, S. J. Billinge, T. Vogt and M. G. Kanatzidis, *J Am Chem Soc*, 2002, **124**, 10157-10162.

34. M. Giorgetti, S. Passerini, W. H. Smyrl and M. Berrettoni, *Inorg Chem*, 2000, **39**, 1514-1517.

35. A. V. Murugan, *Electrochimica Acta*, 2005, **50**, 4627-4636.

36. A. V. Murugan, B. B. Kale, C.-W. Kwon, G. Campet and K. Vijayamohanan, *Journal of Materials Chemistry*, 2001, **11**, 2470-2475.

37. A. V. Murugan, C. W. Kwon, G. Campet, B. B. Kale, A. B. Mandale, S. R. Sainker, C. S. Gopinath and K. Vijayamohanan, *The Journal of Physical Chemistry B*, 2004, **108**, 10736-10742.

38. P. Aldebert, H. W. Haesslin, N. Baffier and J. Livage, *Journal of Colloid and Interface Science*, 1984, **98**, 478-483.

39. X. Crispin, F. L. E. Jakobsson, A. Crispin, P. C. M. Grim, P. Andersson, A. Volodin, C. van Haesendonck, M. Van der Auweraer, W. R. Salaneck and M. Berggren, *Chemistry of Materials*, 2006, **18**, 4354-4360.

40. D. A. Mengistie, M. A. Ibrahem, P. C. Wang and C. W. Chu, *ACS Appl Mater Interfaces*, 2014, **6**, 2292-2299.

41. G. Silversmit, D. Depla, H. Poelman, G. B. Marin and R. De Gryse, *Journal of Electron Spectroscopy and Related Phenomena*, 2004, **135**, 167-175.

42. A. Mendiboure, C. Delmas and P. Hagenmuller, *Journal of Solid State Chemistry*, 1985, **57**, 323-331.

43. L. Athouël, F. Moser, R. Dugas, O. Crosnier, D. Bélanger and T. Brousse, *The Journal of Physical Chemistry C*, 2008, **112**, 7270-7277.

44. M. R. Lukatskaya, O. Mashtalir, C. E. Ren, Y. Dall'Agnese, P. Rozier, P. L. Taberna, M. Naguib, P. Simon, M. W. Barsoum and Y. Gogotsi, *Science*, 2013, **341**, 1502-1505.

45. S. Fleischmann, J. B. Mitchell, R. Wang, C. Zhan, D.-e. Jiang, V. Presser and V. Augustyn, *Chemical Reviews*, 2020, **120**, 6738-6782.

46. X. Shan, F. Guo, D. S. Charles, Z. Lebens-Higgins, S. Abdel Razek, J. Wu, W. Xu, W. Yang, K. L. Page, J. C. Neuefeind, M. Feygenson, L. F. J. Piper and X. Teng, *Nat. Commun.*, 2019, **10**, 4975.

47. X. Shan, F. Guo, K. Page, J. C. Neuefeind, B. Ravel, A. M. M. Abeykoon, G. Kwon, D. Olds, D. Su and X. Teng, *Chemistry of Materials*, 2019, **31**, 8774-8786.

48. T. Sarkar, P. Kumar, M. D. Bharadwaj and U. Waghmare, *Phys. Chem. Chem. Phys.*, 2016, **18**, 9344-9348.